International Journal of Heat and Mass Transfer 161 (2020) 120262

Contents lists available at ScienceDirect

International Journal of Heat and Mass Transfer

journal homepage: www.elsevier.com/locate/hmt

Computational prediction of key heat transfer mechanisms and hydrodynamic characteristics of critical heat flux (CHF) in subcooled vertical upflow boiling

Jeongmin Lee[a], Lucas E. O'Neill[b], Issam Mudawar[a,1,*]

[a] Purdue University Boiling and Two-Phase Flow Laboratory (PU-BTPFL), School of Mechanical Engineering, Purdue University, 585 Purdue Mall, West Lafayette, IN 47907, USA
[b] Creare LLC, 16 Great Hollow Road, Hanover, NH 03755, USA

ARTICLE INFO

Article history:
Received 8 June 2020
Revised 16 July 2020
Accepted 24 July 2020
Available online 14 August 2020

Keywords:
Two-phase flow
Subcooled flow boiling
CFD
Critical heat flux

ABSTRACT

The present study investigates extensively the capability of computational fluid dynamics (CFD) to predict two-phase fluid flow and heat transfer characteristics of FC-72 flow boiling in vertical upflow. The computational method performs transient analysis to model the entire flow field and bubble behavior for highly subcooled flow boiling in a rectangular channel heated on two opposite walls at high heat flux conditions of about 81% of critical heat flux (CHF). Transient variations of local vapor fraction, thermal energy transfer and concentration, and wall temperature are estimated through the computational methodology based on the Volume of Fluid (VOF) approach combined with shear-lift modeling to overcome a fundamental weakness in modeling multiphase flows. Detailed information about bubble distribution in the vicinity of the heated surface, thermal conduction inside the heating wall, local heat fluxes passing through the solid-fluid interface, and velocity and temperature profiles, which are not easily observed or measured by experiments, is carefully evaluated. Predictions are compared to the experimental data for three sets of operating conditions. Overall, computationally predicted flow pattern, bubble behavior, and heat transfer parameters (such as wall temperature excursion and thermal energy concentration) clearly represent phenomena of premature CHF which take place slightly earlier than actual operating conditions. But, despite these slight differences, the present computational work does demonstrate the ability to effectively predict the severe degradation in heat transfer performance commonly encountered at heat fluxes nearing CHF.

1. Introduction

1.1. Status of phase change heat transfer as a thermal management technology

Over the years, two-phase cooling has come into the spotlight because of increased demand for high heat flux thermal management. A representative example is thermal management of data centers, where application of phase change heat transfer has grown considerably due to rapid technological innovation driving adoption of higher capacity cooling approaches. In addition to traditional data center applications of high-performance computing, cloud computing, cellular data processing, and artificial intelligence (AI) applications have further increased demand for computing capacity. With this increase in traffic has come a need to retrofit existing systems with higher-performance hardware requiring higher energy-density cooling schemes, such as two-phase cooling.

Two-phase cooling also trades well for applications in consumer electronics and aerospace sectors due to its inherent ability to provide high flux cooling with minimal added mass and volume. This is made possible by phase-change processes central to two-phase heat transfer (such as evaporation and nucleation) which offer high heat transfer coefficient and maximize a fluid's thermal transport capacity by utilizing latent heat. Because of these benefits, two-phase cooling becomes an attractive option for any application facing increased energy removal requirements.

Two-phase cooling requires understanding of two key processes: boiling and condensation. Boiling is often considered the more complicated phenomenon due to the range of mechanisms by which the fluid may remove heat from a given surface depend-

* Corresponding author.
E-mail address: mudawar@ecn.purdue.edu (I. Mudawar).
[1] Website: https://engineering.purdue.edu/BTPFL.

https://doi.org/10.1016/j.ijheatmasstransfer.2020.120262
0017-9310/

Nomenclature

C_L	shear-lift coefficient
Δc	cell size
d	diameter
E	energy per unit mass
F	force
F_{sl}	shear-lift force
G	mass velocity
G_s	dimensionless shear rate
g	gravitational acceleration
H	height of flow channel's cross-section
h	heat transfer coefficient
h_{fg}	latent heat of vaporization; standard state enthalpy
k_{eff}	effective thermal conductivity
L_d	development length of flow channel in experiment
L_e	exit length of flow channel in experiment
$L_{entrance}$	entrance length in computational domain
L_{exit}	exit length in computational domain
L_h	heated length of flow channel
$\dot{m}$	mass transfer
N	time-step; numerical iteration
P	pressure
q''	heat flux
Re	Reynolds number
r_i	mass transfer intensity factor
S_h	volumetric energy source
T	temperature
T_{in}	temperature at channel inlet
t	time
t_s	thickness of solid wall in computational domain
U_r	relative velocity
u	velocity
V	volume
W	width of flow channel

Greek symbols

α	volume fraction, void fraction
θ	contact angle
μ	dynamic viscosity
ν	kinematic viscosity
ρ	density
ϕ	fluid property

Subscripts

b	bubble
c	critical value; breakpoint
f	liquid phase
g	vapor phase
i	index for phase
sat	saturation
sub	subcooling
w	wall

ing on specific combinations of coolant, heat sink geometry, and operating conditions. Dynamic behavior in the form of instabilities, flow regime changes, and other phenomena inherent to boiling heat transfer can also cause rapid changes in pressure drop and heat transfer behavior if not properly designed for. The most dangerous of these events is encountering critical heat flux (CHF), where a small increase in heat flux can lead to a transition from highly efficient nucleation boiling heat transfer to inefficient film boiling, resulting in heated surface temperatures to increase by orders of magnitude. These temperatures often lead to material failure, which is why CHF is commonly referred to as 'burnout'.

Avoiding CHF and its accompanying potential for system failure is a key focus for design engineers considering two-phase cooling systems. Accurate design tools for predicting both complex interfacial behavior and CHF are of paramount importance because of this, and, towards this goal, studies at the Purdue University Boiling and Two-Phase Flow Laboratory (PU-BTPFL) dating back to the mid-1980s have been conducted to address virtually all possible two-phase cooling schemes, including capillary flows [1], pool boiling [2,2], falling liquid films [4–6], macro-channel flow boiling [7–10], micro-channel flow boiling [11–13], jet impingement [14,15], spray cooling [16], as well as hybrid cooling schemes [17].

But despite these efforts as well as others worldwide, most existing predictive tools are highly empiric in nature. On the other hand, recent advancements in two-phase computational methods show potential to provide a highly generalized framework with which prediction of interfacial behavior, including CHF, across a broad range of operating conditions becomes possible.

1.2. Computational fluid dynamics as an enabler of two-phase flow heat transfer technology development

Computational fluid dynamics (CFD) simulations have matured rapidly over the last several decades and are now capable of providing accurate predictions of flow behavior in a wide variety of applications. Despite these advances, predictive tools for two-phase flow and heat transfer have largely remained empirical in nature due to 1) lack of suitable multiphase computational models and 2) extreme computational expense necessary to resolve small length scales present in evaporation and condensation. Recent advances in both multiphase modeling and computing power have alleviated these shortcomings and led many researchers and design engineers to begin leveraging multiphase CFD simulations as effective design tools.

Capture of hydrodynamic interactions between phases is the most critical aspect of accurate two-phase flow boiling CFD simulations. These interactions lead to distortion of liquid-vapor interfaces, including complex phenomena such as breakup, entrainment, and deposition. Phase distribution within computational domains is commonly tracked using one of two classic methods: Lagrangian and Eulerian. In the former, a moving mesh follows discrete fluid elements within a continuous, moving fluid body. This method allows for very accurate prediction of interfaces but comes with high computational expensive. The Eulerian method, meanwhile, tracks liquid and vapor motion using a fixed grid. This significantly reduces computational expense while still offering relatively good predictive accuracy, leading to its wide adoption in numerous commercial CFD packages.

Researchers are actively exploring alternative approaches to tracking phases within a computational domain. Notable among these are Arbitrary Langrangian-Eulerian approaches (ALE) [18,19], which combines the two classic methods to provide highly accurate predictions by re-meshing at every time step to provide high grid-resolution at phase interfaces. This incurs extreme computational expense, rendering the approach computationally intractable without access to significant high-performance computing resources.

Another alternative approach gaining popularity with contemporary researchers is Lattice Boltzmann Methods (LSMs). Unlike traditional CFD, LSM-based simulations rely on molecular dynamics at their root. They offer high predictive accuracy in cases where stable simulations are possible, but struggle to simulate problems with high density ratios (such as room-temperature boiling with common refrigerants). Nonetheless, LSM has recently been used to simulate flow boiling behavior, including bubble growth and departure [20].

Table 1
Summary of computational approach literature relating to critical heat flux (CHF) prediction.

Author(s)	Geometry dimension (mm)	Fluid	Boundary conditions				Mesh	Model
			ΔT_{sub} (°C)	G (kg/m^{2}s)	q'' (kW/m^2)	P(kpa)		
Pothukuchi et al. [23]	d = 10, 14.9 L = 7000	Water	10	1484.2 – 1993.6	696 - 913	7000	12000 (10 × 1200)	E-E WHFP (α_c = 0.9, 0.95) RNG k-ε
Li et al. [24]	d = 4 - 16 L = 1000	Water	6, 10	1000 - 4000	2359, 3364	7000 - 16000	20 × 400	E-E WHFP (α_c = 0.74, 0.82, 0.9) k-ε
Youchison et al. [25]	W = 40 H = 5 L = 100	Water	92	0.169	- 2600	2000	460,000 – 1,000,000	E-E WHFP (α_c = 0.75) k-ε
Mimouni et al. [26]	d = 6 – 10	Water	0 - 75	2000 - 5000	2450 - 9800	9800 17600	Δc_{max} = 10 mm Δc_{min} = 0.25 mm	E-E WHFP (α_c = 0.82) k-ε
Vyskocil & Macek [27]	d = 8 L = 800, 1000	Water	16 - 323	2000	1250 - 5400	15700	800 × 20	E-E WHFP (α_c = 0.8)
Li et al. [28]	d = 15.4, 15.8 L = 2000, 2750	Water R-113	60 30.3	900 579	570 79.4	4500 2690	10000, 40000 9854, 39416	E-E WHFP (α_c = 0.9, 0.95) SST k-ω

In addition to tracking motion and interactions between phases, accurate modeling of phase change mechanisms is critical to accurate simulation of two-phase cooling. Different models exist to capture phase change, each with unique strengths and weaknesses. One of the most common is the Lee mass transfer model [21] which uses a mechanistic approach and can predict phase change both at interfaces and within bulk phases. Another popular model was developed by Schrage [22] and provides more accurate predictions of mass transfer, albeit only at existing liquid-vapor interfaces. Because of this limitation it is commonly employed to predict phase change in regimes with well-defined interfaces (such as slug and annular flow). To obtain sharp interfaces, interface reconstruction algorithms, which are as important as phase-change and interface tracking methods, are also used, being combined with a phase change model.

Table 1, providing a summary of prior works focused on use of computational methods to predict CHF, shows the most common computational approach is the Euler-Eulerian (E-E) [29,30] two-fluid model. This model solves mass, momentum, and energy conservation equations for each phase, with a shared value of pressure across phases. It relies on specific sub-models for prediction of CHF, the most common of which is the Wall Heat Flux Partition (WHFP) model. This model partitions heat transfer at the wall into components for single-phase liquid convection, evaporation, quenching, and single-phase vapor convection. Partitioning fraction depends on local cell void fraction, with a critical vapor fraction (α_c) set after which single-phase vapor convection dominates. This break point is dependent on operating conditions and anticipated flow regime and is arbitrarily determined for an unknown case.

While formulation of this model is physically based, its reliance on closure correlations (such as the 'critical vapor volume') means it is not always accurate. Further, use of numerous closure correlations throughout the model formulation (including flow regime, liquid-vapor interactions, and other key parameters) leaves the approach's accuracy highly dependent on application to conditions for which its closure correlations are all valid. In more novel configurations (such as heat transfer in micro-gravity), the model is currently ill-suited to offering accurate predictions, and a more fundamental approach is required.

1.3. Objectives of present study

The present study explores use of computational methods to explore flow boiling of dielectric FC-72 in vertical upflow with the aim of investigating flow field behavior just prior to and during CHF. Computational methods include use of additional modeling of shear-lift force (implemented as a User Defined Function (UDF)) acting on vapor bubbles to best capture nucleation, bubble departure, and vapor accumulation in the near-wall region, critical to accurate capture of CHF. A full 3-D computational domain with heated copper walls matching experiment is used to allow comparison of computational results with experimental data.

Three different mass velocities with heat fluxes corresponding to ~81% of CHF are investigated since this is where degradation of nucleate boiling occurs prior to CHF occurrence. Results are analyzed with an eye to both transient behavior (including local bubble motion, void fraction variations, and unstable wall temperature rise) as well as spatial- and time-averaged parameters for comparison with experimental results. Calculation of thermal conduction and wall-to-fluid heat transfer are analyzed to ascertain which cases are more prone to CHF and what key features of the CHF transient are.

Key goals of this work are:

1) Evaluate the ability of the current computational approach to predict heat transfer and hydrodynamic behavior associated with CHF, with focus on key transient variations of temperature and flow-field during CHF.
2) Utilize high resolution offered by computational tools to investigate detailed local heat transfer and fluid dynamics during CHF which are difficult to capture using traditional experimental methods.

2. Experimental methods

Experimental results used for verification in the current study were initially gathered as part of a prior work [31]. The test section used to gather experimental data is the Flow Boiling Module (FBM), part of NASA's Flow Boiling and Condensation Experiment

(FBCE). Additional details on the full two-phase flow loop used to gather experimental results may be found in the original work, but details of FBM will be presented here as they are necessary to best understand the computational domain adopted.

Fig. 1 provides images and schematics highlighting key design features of FBM. Fig. 1(a) provides an exploded view highlighting FBM's construction: three transparent polycarbonate plates are clamped between aluminum support plates, with o-rings acting as seals between the polycarbonate plates. The central polycarbonate plate has a rectangular channel milled into its center, forming the test section flow length, while the top and bottom polycarbonate plates have recessed portions to allow insertion of copper heated walls as shown.

Fig. 1(b) provides a schematic of the flow channel, highlighting its 327.9 mm developing length, 114.6 mm heated length, and 60.9 mm exit length. The rectangular channel has adiabatic, transparent side walls 5.0 mm in height and spaced 2.5 mm apart, providing a hydraulic diameter of 3.33 mm.

Fig. 1(c) shows the 114.6 mm heated length is comprised of top and bottom copper walls (spanning the 2.5 mm channel width) with six resistive heaters providing power to each wall. Heaters on each wall are wired electrically in parallel and matched in resistance to provide a uniform heat flux over the heated surface. Type-E thermocouples are embedded into the wall upstream, downstream, and between adjacent heaters, serving as key measurements for determining heat transfer behavior and detecting CHF.

An image of the FBM is provided in Fig. 1(d) with key features highlighted. Experimental results used in the current study correspond to data collected with the FBM mounted in vertical upflow orientation (inlet at the bottom, exit at the top).

Full details on uncertainty analysis may be found in the original study [31], but for the present work it is sufficient to report temperature measurements are made with uncertainty of +/- 0.5^0C, and overall uncertainty in determining heat transfer coefficient is +/- 8%.

3. Computational methods

3.1. Computational sub-models and key constituent equations

The present study uses ANSYS-Fluent v19.2 with a 3-D computational domain, the volume-of-fluid (VOF) approach for multi-phase tracking, and the *k-ω* turbulence model with shear stress transport (SST) to predict flow boiling. Several assumptions are made to simplify this multi-phase problem to something computationally tractable, key among which are:

1) Fluids are incompressible and immiscible since operating pressures are near atmospheric and two-phase choking is not encountered during experiments.
2) Fluid physical property variations with temperature and pressure are neglected as these are minor over the operating conditions of interest.
3) Heat leaks (determined experimentally to be small) are neglected, the heated surface is assumed to be perfectly smooth, and cavity effects are not considered for nucleation.
4) Surface tension is constant along surface and normal to the interface.

Liquid and vapor phases are tracked throughout the domain by solving the continuity equation using the VOF formulation, which is expressed for each phase as

$$\frac{\partial \alpha_f}{\partial t} + \nabla \cdot \left(\alpha_f \vec{u}_f\right) = \frac{1}{\rho_f} \sum \left(\dot{m}_{gf} - \dot{m}_{fg}\right) \text{ for liquid phase} \tag{1}$$

$$\frac{\partial \alpha_g}{\partial t} + \nabla \cdot \left(\alpha_g \vec{u}_g\right) = \frac{1}{\rho_g} \sum \left(\dot{m}_{fg} - \dot{m}_{gf}\right) \text{for vapor phase}, \tag{2}$$

where α, $\vec{u}$, $\dot{m}$, and ρ are volume fraction, velocity, mass transfer rate, and density, respectively, and subscripts f and g refer to the liquid and vapor phases. The sum of phase volume fractions in a given cell is always equal to unity. Interface reconstruction is handled by a piecewise-linear approach [32] with anti-diffusion treatment in order to provide physical interface shapes within the domain. Gravity is included to account for buoyancy force within the domain. Single mass, momentum, and energy conservation equations are solved for the two phases, using cell-based volume-averaged physical properties. Momentum and energy equations are as follows:

$$\frac{\partial}{\partial t}(\rho \vec{u}) + \nabla \cdot (\rho \vec{u}\vec{u}) = -\nabla P + \nabla \cdot \left[\mu\left(\nabla \vec{u} + \nabla \vec{u}^T\right)\right] + \vec{F}, \tag{3}$$

$$\frac{\partial}{\partial t}(\rho E) + \nabla \cdot (\vec{u}(\rho E + P)) = \nabla \cdot \left(k_{eff} \nabla T\right) + S_h, \tag{4}$$

where P, E, $\vec{F}$, and S_h above refer to pressure, specific internal energy per mass, and source terms. Surface tension force is included as a source term in the momentum equation, using the continuum surface force (CSF) model proposed by Brackbill et al. [33]. Wall adhesion is also taken into account, using contact angle with a wall to adjust the local surface curvature near the wall, which is used to calculate the resulting surface tension force. While the surface normal in CSF is determined by gradient of volume fraction of phases, the normal direction for wall adhesion force is computed by

$$\hat{n} = \hat{n}_w \cos\theta_w + \hat{t}_w \sin\theta_w, \tag{5}$$

where $\hat{n}_w$ and $\hat{t}_w$ are, respectively, the unit normal and tangential vectors relative to the wall. In the present study, 175^0 is used as contact angle, defined from the inside of a vapor bubble to the liquid-vapor interface. Contact angle is important as it directly impacts adhesion of bubbles to the heated surface, affecting bubble lift-off diameter and thus heat removal during nucleate boiling. As mentioned previously, the two-equation *k-ω* SST model with turbulence dampening is employed to account for turbulent effects during flow boiling. Influence of turbulence model on two phase flow predictions was discussed extensively in a previous study [34].

Another important parameter for effective capture of flow boiling behavior is shear-lift force. Discussed extensively in a prior work [35], the current approach with VOF and PLIC + CSF is deficient in resolving local shear-stress for bubbles moving in bulk liquid flow, particularly in the case of bubble motion in a liquid boundary layer. In this situation, shear-lift force is expected to drive bubble motion away from the wall and into bulk liquid flow. Accurate prediction of this process is key to resolving boiling heat transfer in the near-wall region. To rectify this shortcoming, the present authors included a UDF to better account for shear-lift force, using the correlation of Klausner et al. [36] as its basis. This correlation was developed using data for a wide range of Reynolds numbers and is given as

$$F_{sl} = \frac{1}{8}\pi C_L \rho_f U_r^2 d_b^2, \tag{6}$$

where

$$C_L = 3.877 G_s^{1/2} \times \left[\mathrm{Re}_b^{-m/2} + \left(0.344 G_s^{1/2}\right)^m\right]^{1/m}, m = 4, \tag{7}$$

$$G_s = \frac{1}{2}\left|\frac{dU_r}{dy}\right|\frac{d_b}{U_r}, \tag{8}$$

G_s is the dimensionless shear stress based on relative velocity between vapor and liquid phases, and Re_b is bubble Reynolds number based on bubble diameter as characteristic length.

Calculation procedure for implementing this as a UDF is depicted in Fig. 2. As it is numerically expensive to evaluate every

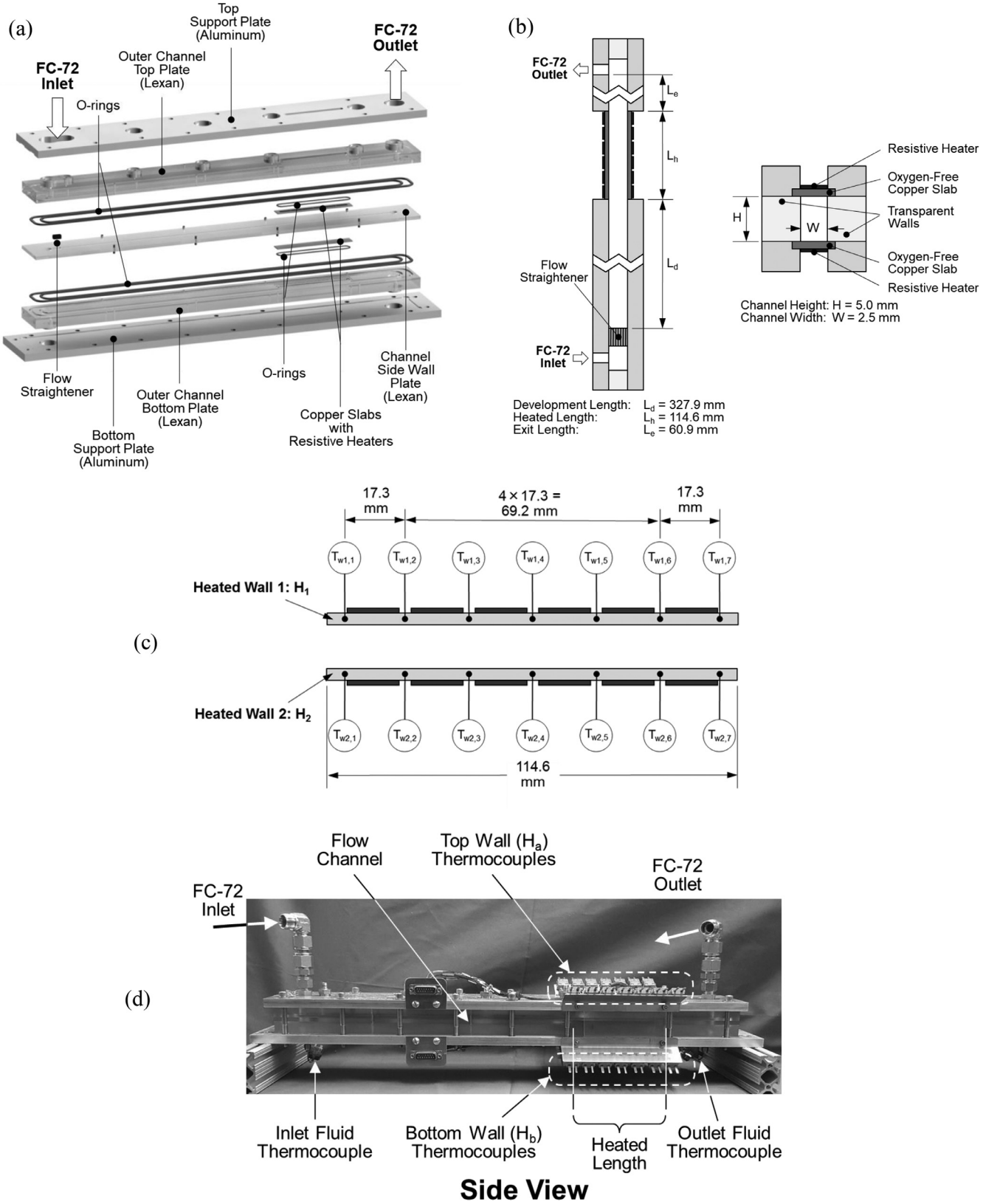

Fig. 1. (a) Exploded view showing Flow Boiling Module (FBM) construction. Schematics of (b) FBM fluid passages and (c) heated length instrumentation. (d) Image of FBM with key features highlighted.

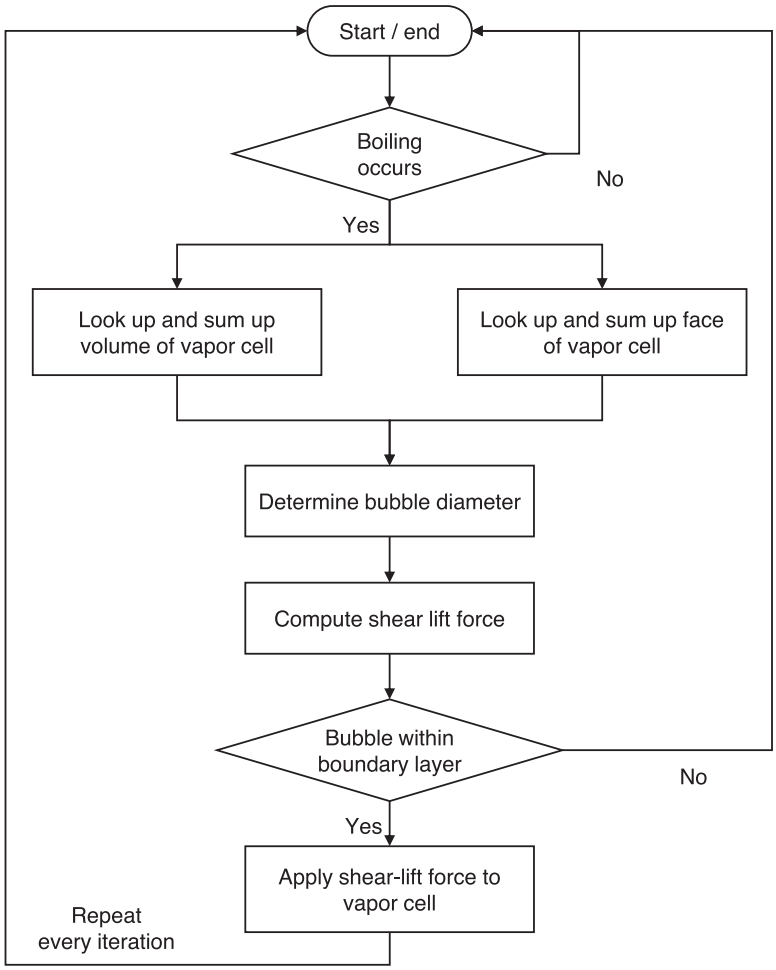

Fig. 2. Schematic of process of computing and applying shear-lift force.

bubble individually, average bubble parameters corresponding to inlet, middle, and exit regions are used to determine the magnitude of source terms. Similarly, liquid and vapor velocities are averaged in each region to determine velocity difference between phases. It should also be noted that shear-lift force is only applied to bubbles within the boundary layer, as it is expected to approach zero in the free-stream, and accounts for gradients in streamwise (z-direction) velocity, as transverse velocity gradients are minimal. More detailed information on rationale and verification of the shear-lift force UDF may be found in the previous study [35].

Phase change modeling is also critical to ensuring accurate prediction of flow boiling heat transfer and fluid dynamics. The Lee mass transfer model is used in the current work, as the authors have previously validated its performance under similar operating conditions. Although less accurate than alternative models, it can predict phase change in the absence of existing interfaces (e.g., within bulk phases), allowing it to approximate nucleation and bubble growth in the near-wall region. Mass transfer is calculated according to the following relations:

$$\dot{m}_{fg} = r_i \alpha_f \rho_f \frac{\left(T_f - T_{sat}\right)}{T_{sat}} \text{for evaporation,} \tag{9}$$

$$\dot{m}_{gf} = r_i \alpha_g \rho_g \frac{\left(T_{sat} - T_g\right)}{T_{sat}} \text{for condensation,} \tag{10}$$

where r_i is the mass transfer intensity factor. This value must be tuned depending on boundary conditions as it affects vapor growth rate within the domain. Identical values of mass transfer intensity factor for both evaporation and condensation have been widely used for near-saturated flow boiling in channels with small hydraulic diameter and low mass velocity.

However, tuning of r_i values should be carefully conducted for situations involving highly subcooled flow boiling, relatively large diameter, low fluid thermal conductivity, and high mass velocity. This is because, as thermal boundary layer cannot engulf the flow channel, core region bulk fluid can remain highly subcooled. Large temperature differences between liquid and vapor cells result in significant interfacial thermal energy diffusion, causing difficulty with interfacial tracking and accelerating the rate of vapor bubble condensation in a non-physical manner. Moreover, vapor bubbles are typically generated in cells near the heated wall, mostly within the subcooled liquid's viscous sublayer. Within this layer, heat is transferred by diffusion rather than convection (including advection), and weak thermal diffusion (due to the fluid's low thermal conductivity) cannot induce vapor bubble growth for a given time step in the transient analysis if identical r_i values are used. Therefore, different values of r_i are employed in the current work, 100 for evaporation and 0.1 for condensation. Use of these values has been validated in the authors' prior work [35], which examined the influence of r_i values on vapor bubble formation along the channel.

Material properties throughout the domain are calculated based on the vapor fraction in each cell. Mathematically this equates to

$$\phi_i = \alpha_g \phi_g + (1 - \alpha_g)\phi_f, \tag{11}$$

where ϕ is any material property (*e.g.,* density, thermal conductivity) and α is volume fraction.

3.2. Computational domain, and initial/boundary conditions

The present study simulates subcooled flow boiling of FC-72 through a 2.5 mm x 5 mm rectangular channel 129.6 mm in length (corresponding to the heated length of the FBM described in Fig. 1 with a 5 mm entrance length and 10 mm exit length). Fig. 3 shows details of the computational domain used, which is 3-D, full-scale, and uses only structured (cartesian) elements. Heated copper walls are also included in the computational domain to allow simulation of conjugate heat transfer, with physical dimensions of 2.5 mm x 1.04 mm x 114.6 mm, corresponding exactly to experimental conditions (critical to capture conduction within the heated walls). Computational grid refinement in the near-wall region is used to best capture key fluid dynamics and heat transfer in this region, primarily vapor growth and departure. Total number of cells in the mesh is 1.87 million, with a minimum cell height of 6.5 μm used in the near-wall region. Grid independence and y^+ values for this domain were verified in a prior study [35].

Three different combinations of mass velocity and heat flux are investigated, all corresponding to vertical upflow orientation. Mass velocities range between 176.52–2432.51 kg/m^{2}s, heat fluxes between 189.90–361.15 kW/m^2 (corresponding to 78–84% of CHF), and inlet subcooling from 30.81 to 36.18 °C. Fully developed, single phase velocity profiles corresponding to each mass velocity are applied as inlet boundary conditions (including values of turbulent kinetic energy and dissipation). Heat flux values applied are uniform over outer surfaces of the copper walls, and side walls are considered adiabatic (both in agreement with experimental methods employed as described in Section 2).

In order to improve computational stability and reduce computational time, steady-state results from a prior study corresponding to identical flow conditions at lower heat fluxes (42 – 45% of CHF) are used as initial conditions for corresponding cases in the present study. Variable time-step size is used, ranging from 10^{-7} to 10^{-5} s while satisfying a global Courant number ($u\Delta t/\Delta c$) criterion of unity for numerical stability. Physical properties, full numerical details and discretization details are presented in Tables 2 and 3.

4. Results and discussion

The current methodology was validated in prior studies [34,35] by comparing predictions for heat flux of ~45% CHF with experimental data for flow regime and local heat transfer. In the present study, transient simulations are again performed to assess the ability of the aforementioned computational scheme to predict flow boiling of FC-72, this time at very high heat fluxes (~81% of CHF) corresponding to the upper portion of the nucleate boiling region where heat transfer degradation occurs as heat flux approaches CHF. Vapor distribution along both streamwise and transverse directions, wall conduction effects, and transient temperature variations are all systematically investigated.

Unlike the prior simulations, which resulted in steady-state results at low heat flux levels, the present set of boundary conditions and computational scheme result in 'pre-CHF' conditions observed in the computational domain. This refers to vapor accumulation in the near-wall region leading to reduced heat transfer and rapid, unsteady temperature rise. The following subsections will investigate this behavior further to offer key insights on local heat transfer behavior in the lead-up to and during the CHF transient.

Table 2
Thermophysical properties used in computational model.

G (kg/m^{2}s)	T_{sat} (°C)	h_{fg} (J/kg mol)	ρ_f (kg/m^3)	c_{pf} (J/kg · K)	k_f (W/m · K)	μ_f (kg/m · s)	ρ_g (kg/m^3)	c_{pg} (J/kg · K)	k_g (W/m · K)	μ_g (kg/m · s)	σ (N/m)
176.52	61.97	2.775×10^7	1608.8	1117.1	0.0536	3.858×10^{-4}	15.874	942.06	0.0142	1.209×10^{-5}	0.0080
445.75	60.16	2.761×10^7	1605.2	1120.1	0.0534	3.786×10^{-4}	16.591	946.91	0.0143	1.215×10^{-5}	0.0079
2432.51	69.37	2.701×10^7	1589.6	1133.1	0.0527	3.497×10^{-4}	19.953	967.97	0.0149	1.243×10^{-5}	0.0073

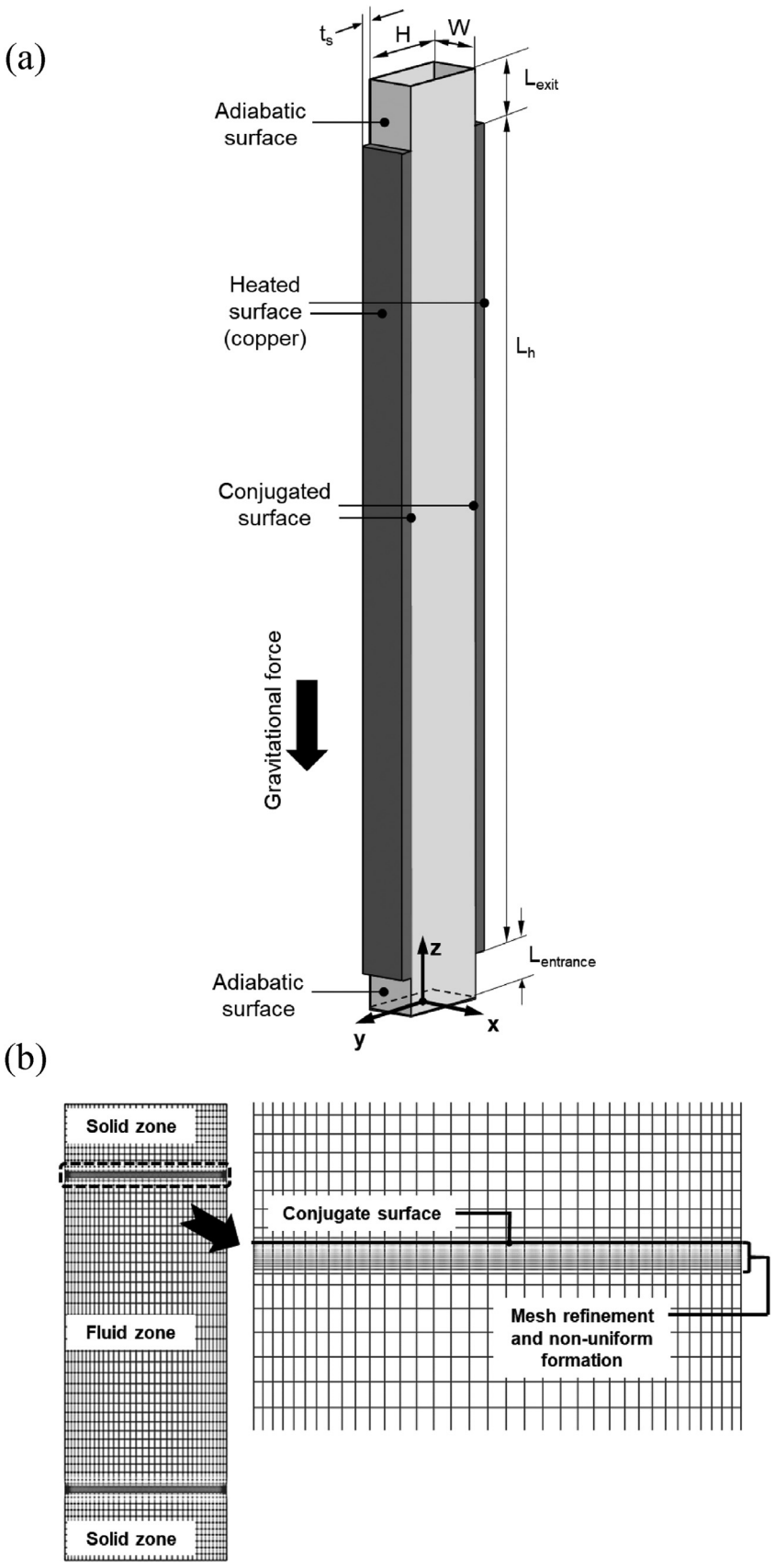

Fig. 3. (a) Schematics of 3-D computational domain and (b) details of mesh on cross section area.

Table 3
Numerical details and discretization methods.

Pressure-velocity coupling	Pressure-implicit with splitting of operators (PISO)
Gradient	Least square cell based
Pressure	PRESTO!
Momentum	Third-order monotonic upstream-centered scheme for conservation laws (MUSCL)
Volume fraction	Geo-reconstruct
Turbulent kinetic energy	First-order upwind
Specific dissipation rate	First-order upwind
Energy	Second-order upwind
Transient formulation	First-order implicit

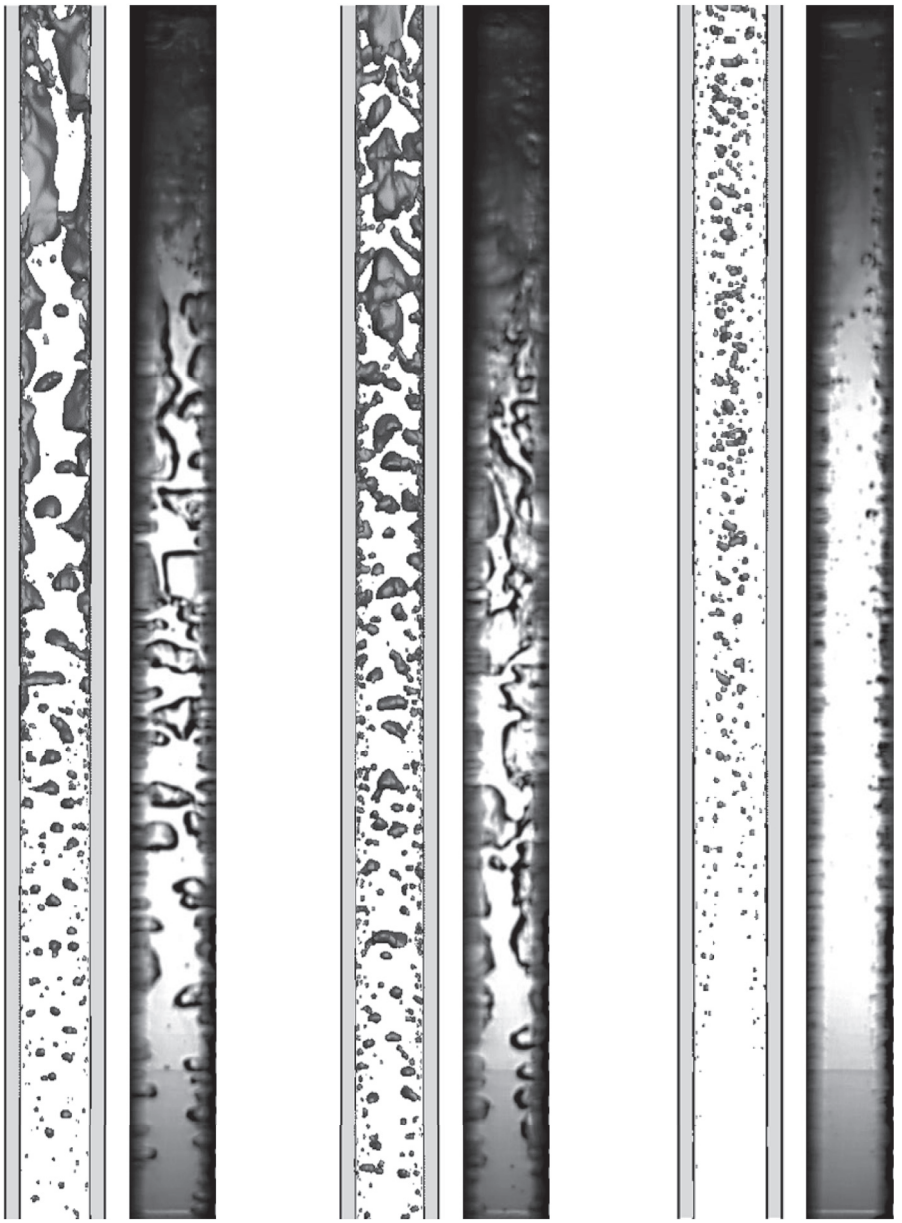

Fig. 4. Comparison of flow visualization from experiment with predictions of transient 3-D computational approach for three different cases.

4.1. Predicted two-phase flow liquid/vapor distribution leading to wall temperature escalation

It is important to validate that computationally predicted two-phase flow configurations at high heat fluxes follow the trend of experimental observations for flow regimes observed just before CHF. Extreme care must be taken as temperature excursion occurs quickly once local conditions become such that vapor production prevents liquid access to the heated wall, an event which may occur within the space of a single computational time step. Fig. 4 shows flow visualization results predicted by the current computational method compared with those captured for identical experimental conditions. These correspond to mass velocities of G = 176.52, 445.75, and 2432.51 kg/m^{2}s, all with heat flux ~81% of CHF. Individual images showcase how similar vapor shape and interfacial behavior is for both predicted and experimental results. It is important to note here that results for the two lowest mass velocity cases (G = 176.52 and 445.75 kg/m^{2}s) are not steady, and transient analysis shows they are likely undergoing CHF. This will be discussed in more detail later in this section.

Key features of highly subcooled flow boiling depicted in Fig. 4 are vapor growth, bubble departure, coalescence, break-up, and condensation. Results shown here correspond to inlet subcoolings of 30.81 to 36.18 °C. In each case, flow is hydrodynamically fully developed by the beginning of the heated length, and boiling initiates as micro-bubbles are formed near the leading edge of the heated length. Computationally, generation of vapor is determined by the size of cells adjacent to the heated wall, with smaller cells

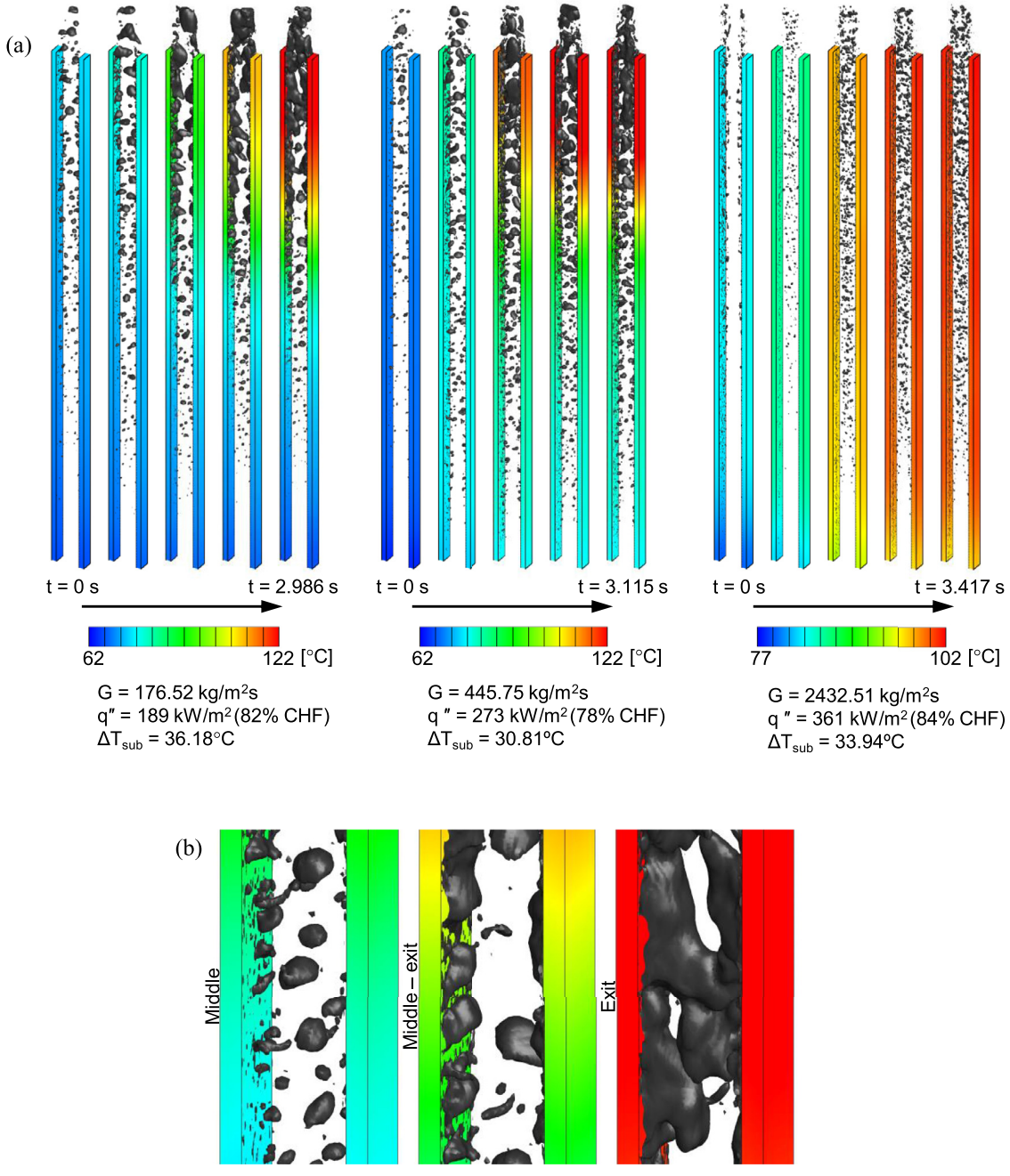

Fig. 5. (a) Computationally obtained bubble formation images and wall temperature distribution of entire heated channel for different mass velocities and different heat fluxes (but similar heat flux percentage of CHF), and (b) magnified bubble formations at different locations in the end of computing time for G = 176.52 kg/m^{2}s.

providing higher resolution and more physical vapor production. Grid refinement was a major focus of the authors' prior work and the present computational domain is sufficiently refined to offer accurate predictions.

Fig. 4 shows computational simulations generally succeed in mirroring experimental results, but some local predictions of interface behavior show slightly different behavior. For the two lowest mass velocity cases, key boiling behavior including bubble coalescence, vapor layer waviness, and coalescence in the downstream region are well captured by the current computational approach. Bubble formation, lift, and entrainment are well-captured in the upstream portion of the channel and, moving along the streamwise direction, it is clear coalescence and wavy vapor layer dynamics are also well captured. For all cases, vapor growth is present along the full length of the heated wall. In the downstream region, incoming vapor formed upstream merges with bubbles growing on the heated wall to form large liquid slugs which then move towards the vapor core. This migration towards the channel center occurs for smaller bubble sizes at higher mass velocities, due to the increased influence of shear-lift force at higher mass velocities (both from heated walls and adiabatic side walls).

To complement the qualitative comparison of computational and experimental results provided in Fig. 4, Fig. 5 offers detailed local results showcasing the evolution of local flow features. Fig. 5(a) shows how the flow-field evolves with computational time (increasing number of time steps), while Fig. 5(b) provides detailed views of vapor distribution at different locations along the channel length corresponding to steady-state results for the lowest mass velocity case. A variable time stepping approach was employed here, and, as an interesting intersection between physics and computational methods, a smallest time step was required for the lowest mass-flux case due to the significant impact of flow acceleration. The highest mass velocity case, meanwhile, saw the least change in void fraction along its length, and employed the largest average time step of the three cases assessed.

In each case shown in Fig. 5(a), simulations are started using results for a lower heat flux which leads bubbly flow to be the dominant flow regime along the channel. As additional time steps are taken (N increases), phase change accelerates due to the higher heat flux leading to more rapid bubble growth and more vapor coalescence along the channel. Small, near-spherical bubbles characteristic of bubbly flow are replaced by large, elongating vapor pockets characteristic of higher void-fraction flows. Shear stress, buoyancy, turbulence, and other hydrodynamic phenomenon act locally to influence vapor motion, and, near the channel exit, are seen to result in break-up of large vapor structures formed upstream.

These local vapor behaviors along the channel (and their influence on wall temperature) are seen to vary appreciably with mass velocity. For the lower mass velocity cases of $G = 176.52$ and 445.75 kg/m^{2}s, bubbly flow dominates the upstream region, while a continuous vapor layer is seen to form in the downstream portion of the channel. Fig. 5(b) in particular shows the formation of a wavy liquid-vapor interface with clear wetting fronts present near the channel exit. These are all key characteristics of pre-CHF flow [37–40] and help validate the current computational approach's ability to capture these complex phenomena. It should also be noted that wall temperatures in this region are ~120 °C, which in experiments performed with the current setup is commonly seen just before CHF occurs.

To augment visualization results presented in Fig. 5, Fig. 6 provides comparison of experimental and computed wall temperatures. As discussed previously, computational runs are initiated using steady-state results from cases with identical mass velocity and heat flux ~45% of CHF, with the new, higher heat flux applied at time $t = 0$ ($N = 0$ time steps). Fig. 6 highlights evolution of local (computational) wall temperatures with time for each mass veloc-

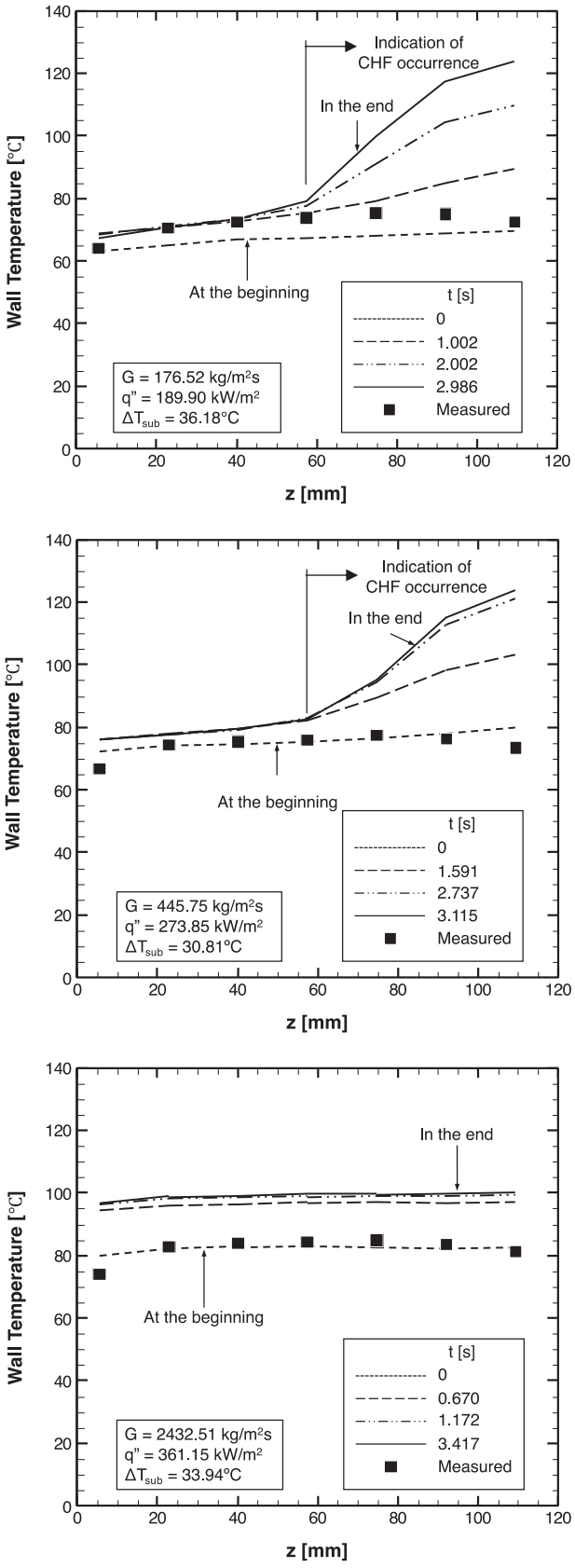

Fig. 6. Comparison of wall temperature variations from experiment with predictions of transient 3-D computational method along the axial coordinate under the indicated operating conditions.

ity (lines), plotted alongside steady, time-averaged measured wall temperatures (squares). These temperatures were measured using thermocouples embedded into the heated wall at axial positions of z = 5.4, 22.7, 40.0, 57.3, 74.6, 91.9 and 109.2 mm from the leading edge as described in Section 2.

For the two lower mass velocity cases of G = 176.52 and 445.75 kg/m^{2}s, simulation results show wall temperatures exceeding those measured experimentally. This difference is very minimal in the upstream portion of the channel, but, as flow moves downstream, computational predictions become much higher than experimental results. This is attributable to the vapor blanketing in the downstream region observed for corresponding cases in Fig. 5, and is a key indicator flow incurring CHF.

The highest mass velocity case in Fig. 6 shows relatively constant temperature along the channel length (showing no signs of temperature excursion as in the lowest two mass velocity cases), but offset from experimental results by ~20 °C. Across all plots in Fig. 6, simulated wall temperatures are seen to exceed those observed experimentally, likely attributable to differences in void fraction magnitude and vapor distribution within the channel. These differences, in turn, are likely attributable to mass transfer intensity factor r_i selected. This will be discussed further in a later subsection.

To further explore these potential sources for temperature discrepancy, Fig. 7 provides plots of area-averaged void fraction versus channel axial position. Similar to temperature plots in Fig. 6, curves are plotted corresponding to different simulation times between initial condition and the end of transient analysis (or steady state in the case of the highest mass velocity). Experimental void fraction results were not attainable for the current conditions (due to difficulty estimating vapor volume for irregular shapes present in vapor structures), but plots in Fig. 7 help better explain temperature discrepancies seen in Fig. 6.

For the two lower mass velocity cases, Fig. 7 shows void fraction is initially under 10% along the entire channel. After the new (higher) heat flux is applied and computational time advances, this value increases along the channel length. Most notable, however, is the significant growth after the midway point in the channel (z ~60 mm); void fraction increases by a factor of ~ 5x by the end of the channel. This significant accumulation of vapor in the downstream region is directly responsible for the large temperature excursions seen in Fig. 6.

Unlike the two lower mass velocity cases, the highest mass velocity cases of G = 2432.51 kg/m^{2}s shows linear variations in void fraction along the channel length, indicating there is no drastic change in vapor accumulation downstream. This agrees well with the near-constant temperature profiles seen for these two cases in Fig. 6, although does not explain why temperature values are higher than those observed experimentally.

Across all three cases investigated here, void fraction remains below ~37%, which, along with visualization results in Fig. 5, indicates flow regime does not approach low liquid content regimes (such as mist flow) which may lead to dryout as the dominant CHF mechanism. This agrees well with experimental results indicating the dominant CHF mechanism is hydrodynamic in nature (i.e., capable of being predicted by the Interfacial Lift-Off Model [38,41]).

Fig. 8 provides additional plots of void fraction along the channel length to further examine the different flow regimes and heat transfer mechanisms indicated in Figs. 6 and 7. Fig. 8(a) shows contours of void fraction along the heated wall for each mass velocity at the initial condition (left) and steady-state (right). Contours for the lowest mass velocity case of G = 176.52 kg/m^{2}s show nucleate boiling dominates in the upstream region, but an abrupt transition to a high void-fraction regime is seen starting near the axial midpoint. Similar behavior is seen for the case with G = 445.75 kg/m^{2}s, reinforcing the trends seen in Figs. 6 and 7.

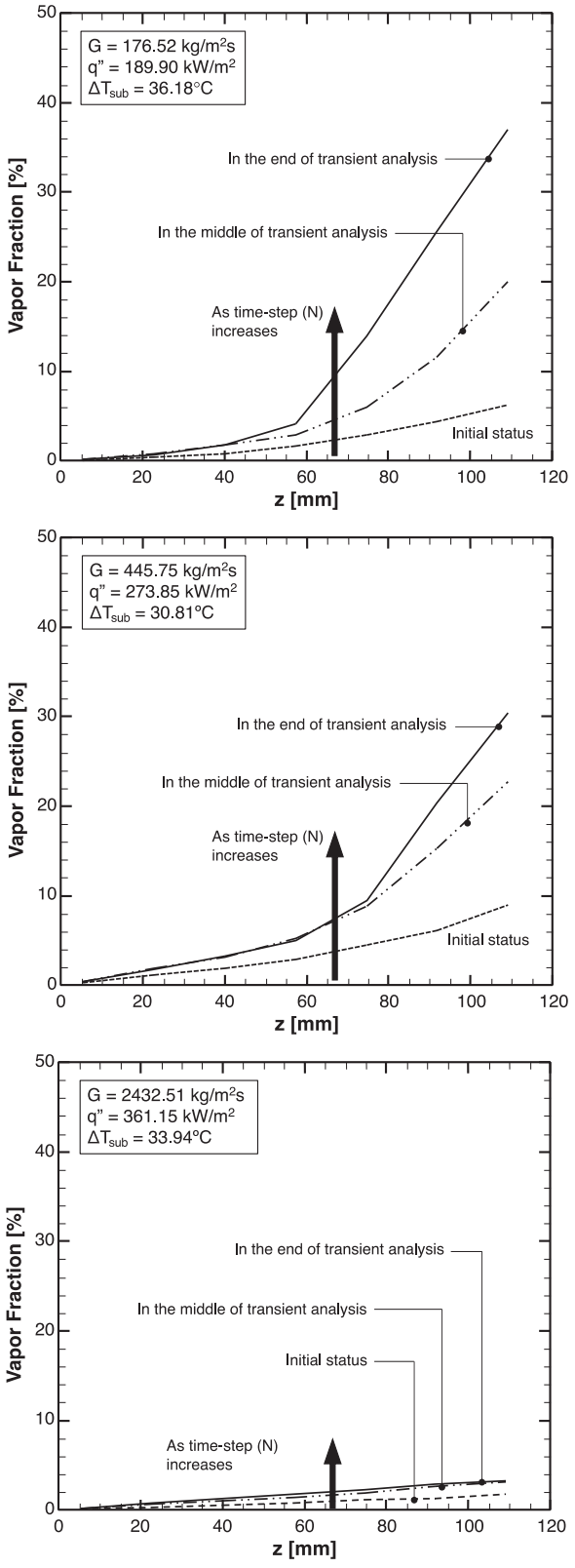

Fig. 7. Transient variations of volume-weighted average of local vapor fraction on the cross-sectional area at different axial locations for three mass velocities, but similar heat flux percentages of measured CHF.

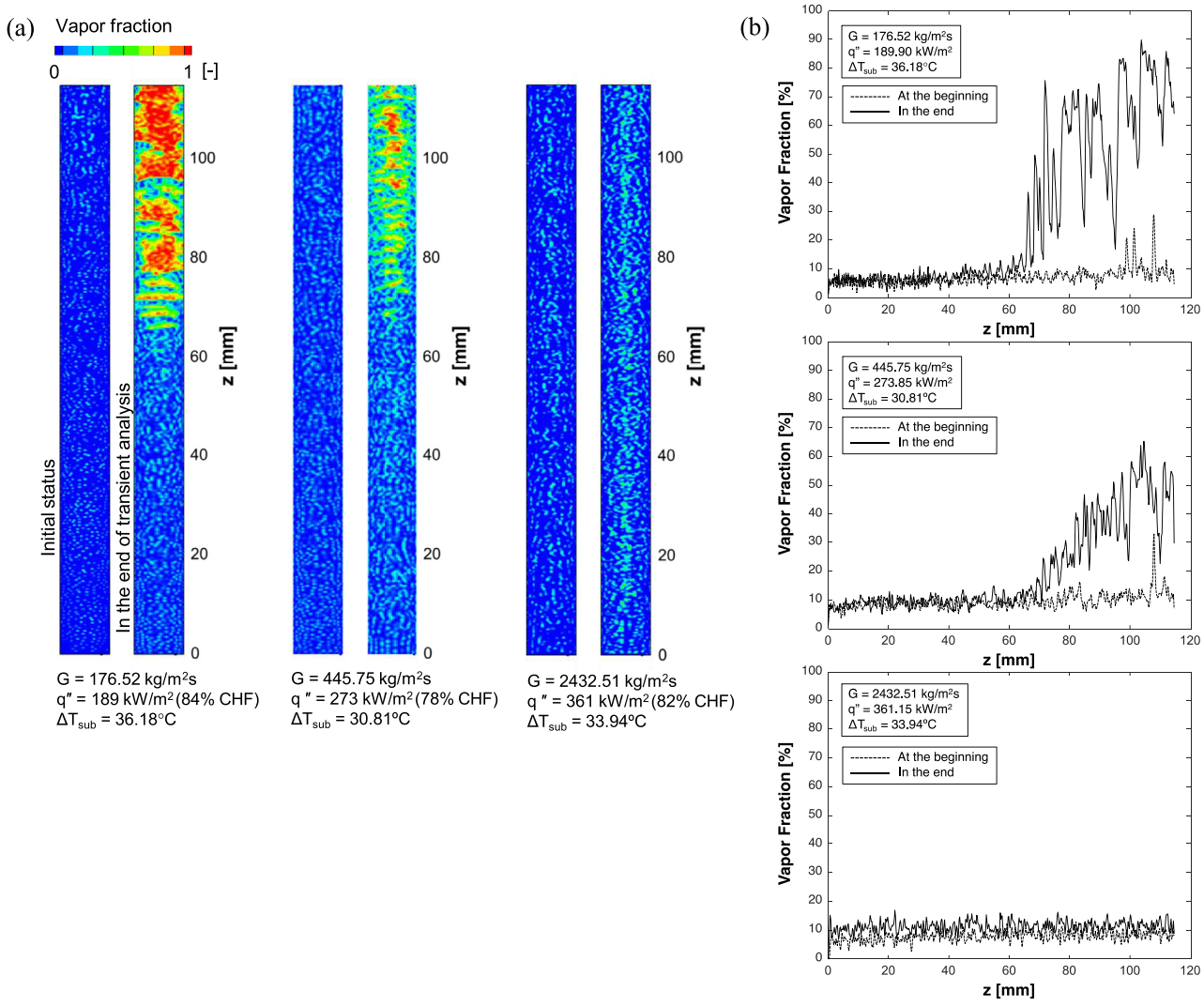

Fig. 8. (a) Contours of vapor fraction along the entire heated surface at the beginning (left) and end (right) of transient simulation for the different mass velocities. (b) Instantaneously captured variations of the spatially averaged vapor fraction with respect to the transverse coordinate (*x*-axis) along the heated portion of the channel.

The highest mass velocity case in Fig. 8(a), meanwhile, shows relatively constant values of void fraction along the heated wall. This indicates vapor generation rate remains constant along the channel length, and bubbles formed along the heated wall continuously depart and enter the bulk flow (note Fig. 8(a) shows only void fraction *at the heated wall*). Comparison with lower mass velocity cases in Fig. 8(a) indicates wall adhesion and sliding is more likely for cases with low flow inertia, a result which is not clearly shown in experimental photos in Fig. 5, but makes physical sense due to the increased role of shear-lift force at high mass velocities.

Also key to note across all cases in Fig. 8(a) is the concentration of vapor towards the channel centerline. This is particularly noticeable for the two highest mass velocity cases, and is due to the role of shear-lift force resulting from boundary layers formed by the channel sidewalls pushing vapor towards the channel centerline. This is yet another physical phenomenon missed in 2-D simulations, illustrating why it is imperative to perform flow boiling simulations in 3-D [34,35].

Fig. 8(b), meanwhile, provides plots of local void fraction averaged across the transverse direction (*x*-axis) along the axial length. These curves are evaluated directly at the wall (corresponding to the contours shown in Fig. 8(a)), and plots are provided for both initial and steady-state results. Plots corresponding to the highest mass velocity case of $G = 2432.51$ kg/m^{2}s show uniform increases in wall void fraction along the channel length, and relatively uniform variation in void fraction throughout the channel length. The two lower mass velocity cases, meanwhile, again show a sharp increase in wall void fraction, indicating both vapor adhesion and boiling rate increase dramatically in the downstream region. Wall void fraction is seen to vary significantly with axial position as well (with void fraction in the lowest mass velocity case varying from ~15% to 90% within a few millimeters), behavior which is not attributable to vapor growth alone. Rather, these results indicate complex behavior including vapor growth, departure, coalescence, and re-attachment to the heated wall are taking place, phenomena which are difficult to observe experimentally.

Across Figs. 5–8 it is apparent the highest mass velocity case of $G = 2432.51$ kg/m^{2}s is fundamentally different from the others investigated. Single-phase liquid convection plays a much more prominent role in heat transfer, and boiling remains in the nucleate regime all along the channel length. Void fraction values are also the lowest for this case due to the decreased residence time of liquid along the heated length, and the fact it reaches a steady-state solution indicates it is not yet nearing CHF. Further discussion of heat transfer mechanisms for each case will be provided in the following section.

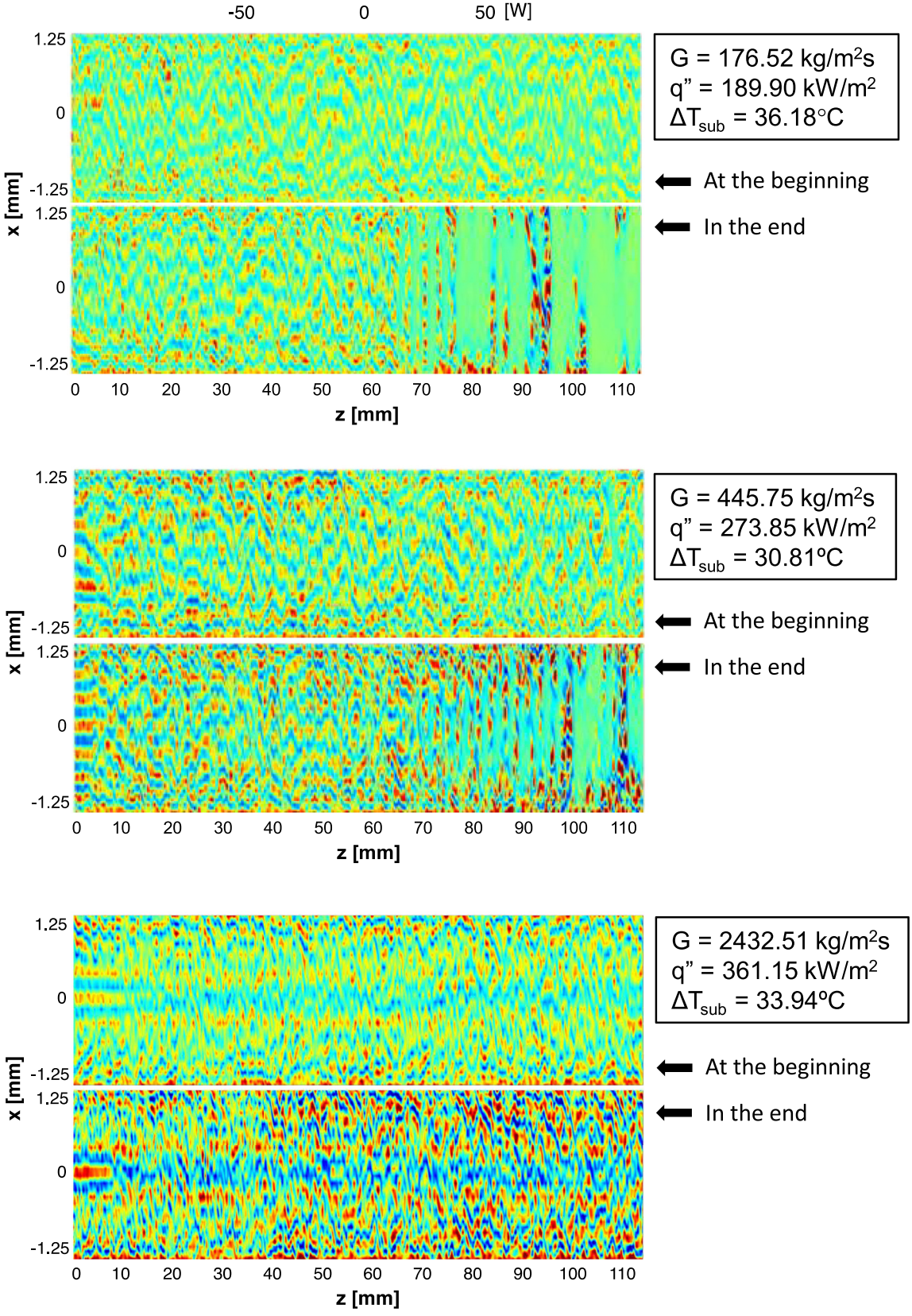

Fig. 9. Contour of the thermal energy transfer induced by thermal conduction on the one of the heated walls with respect to time (numerical time step).

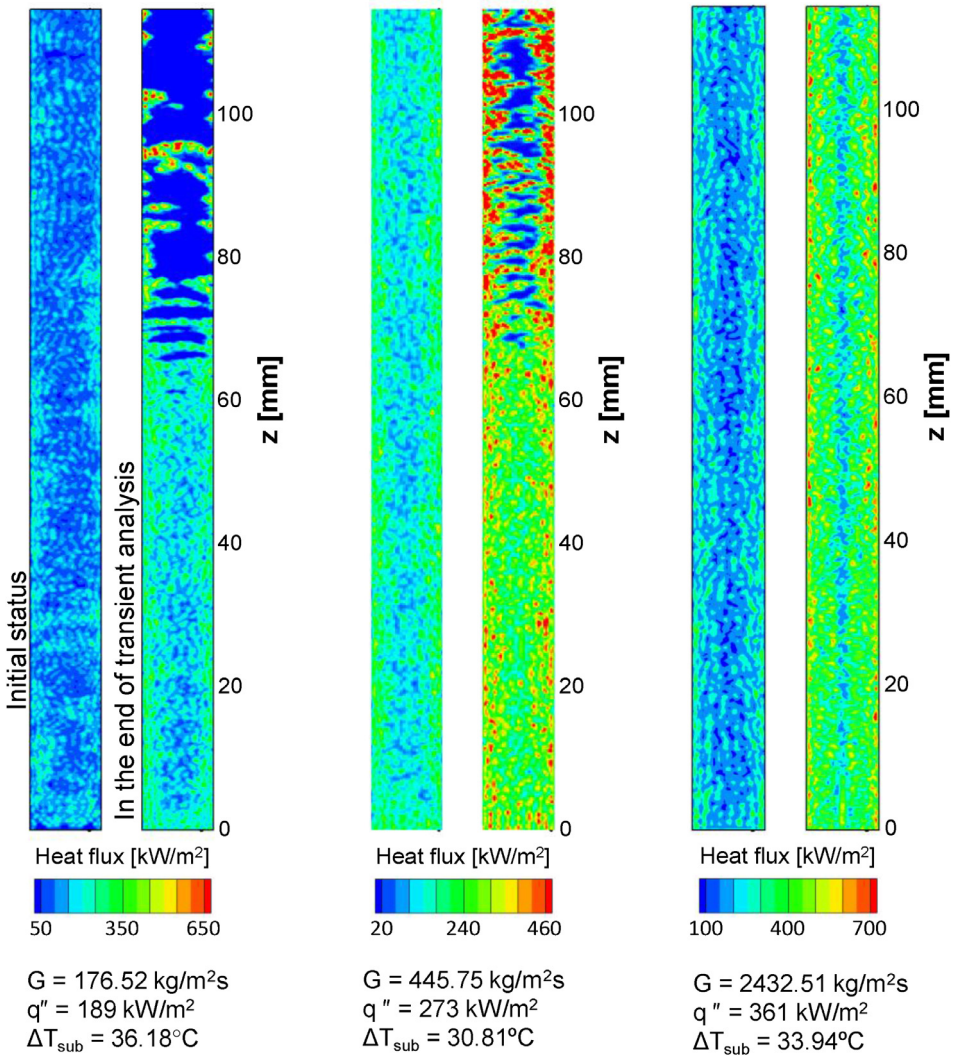

Fig. 10. Contours of heat flux passing through one entire heated surface of the channel, which is captured at the beginning (left) and the end (right) of transient simulation for the different mass velocities.

4.2. Heat transfer characteristics concomitant with aggressive vapor generation

Fig. 9 provides lateral contours of thermal energy transfer (in Watts) in the *x-z* plane, accounting for both axial and lateral heat transfer in one of the heated walls. Thermal energy transfer is defined as thermal energy exchange by conduction between an individual cell and the adjoining cells on the surface of the solid domain. These plots provide a level of detail not available using traditional experimental methods, effectively allowing capture of instantaneous variations in surface heat flux due to boiling. Conduction rate is calculated using nodal temperatures combined with Fourier's Law, and unit depth into the copper solid domain is assumed. In this figure, blue color for a local wall cell indicates thermal energy is lost to surrounding cells, red color gained from surrounding cells, and green color points to regions of the surface where axial and lateral conduction effects are minimal.

For all three mass velocities, Fig. 9 shows the initial condition exhibits minimal differences in local heat transfer, but, as time advances after heat flux is increased, local variations become more pronounced, which points to increased reliance on conduction (evidenced by distinct blue-red leopard pattern) upon reaching CHF for the two lower mass velocity cases or approaching CHF for the highest mass velocity. For the two lower mass velocity cases, broad green areas in the downstream region are indicative of appreciable vapor blanketing, where conduction effects are minimized.

Overall, viewing Figs. 8 and 9 together shows locations with vapor in the near-wall region experience strong local variations in heat transfer due to instantaneous vapor distribution. This reliance on small areas where liquid accesses the heated wall is a key feature of pre-CHF flows: once these final liquid access points are occluded, wall temperature increases rapidly, and CHF begins in earnest.

Similar to Fig. 9, Fig. 10 provides contours of local heat flux at the heated surface for each set of operating conditions investigated. In following with conclusions from Figs. 8 and 9, both the highest magnitudes of heat flux and highest local variation in heat flux can be seen where significant vapor blanketing is observed within the channel. This is again due to reduction in available 'high-efficiency' (boiling) heat transfer surface area, leading to non-uniform energy rejection as compared to that seen for lower heat fluxes.

In all cases shown in Fig. 10, peak heat transfer rates are commonly achieved near the channel sidewalls. This is in agreement with the trend of shear-lift incurred by the sidewalls helping drive vapor towards the channel centerline, providing more opportunity for liquid wetting fronts near channel sidewalls.

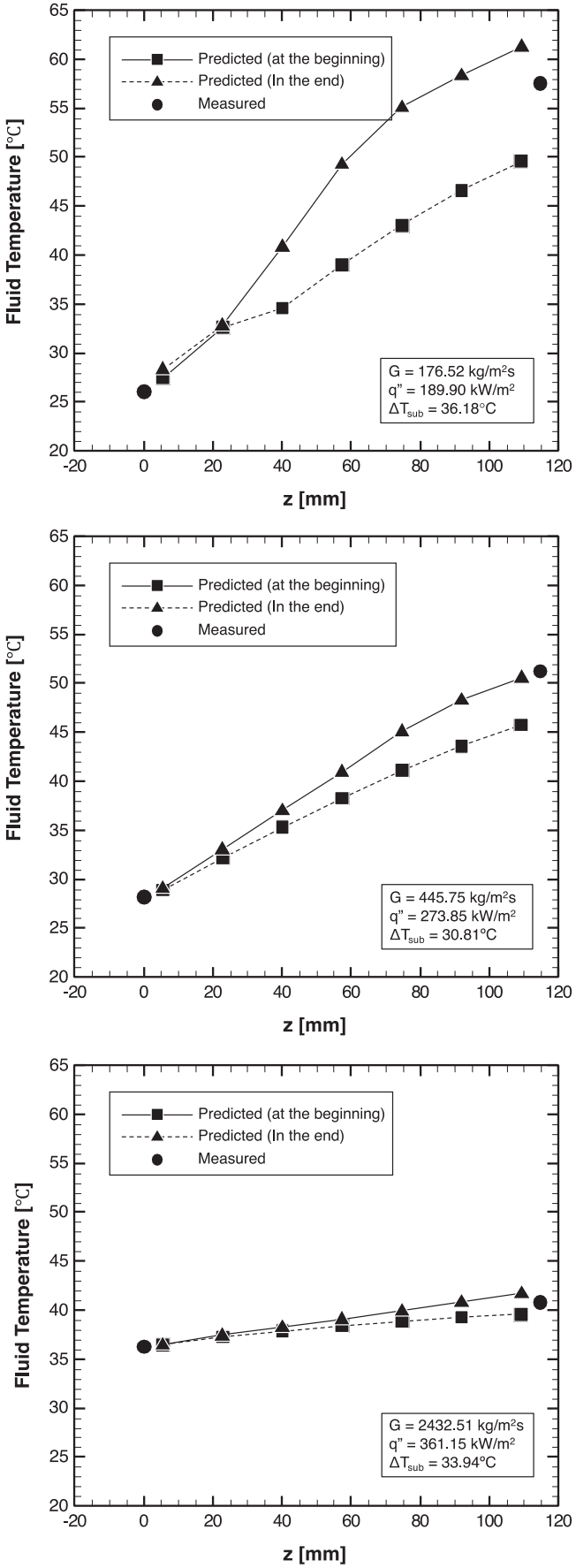

Fig. 11. Instantaneously captured fluid temperature variations with axial coordinate during the transient analysis, and measured inlet and outlet temperature of the flow boiling module for three operating conditions.

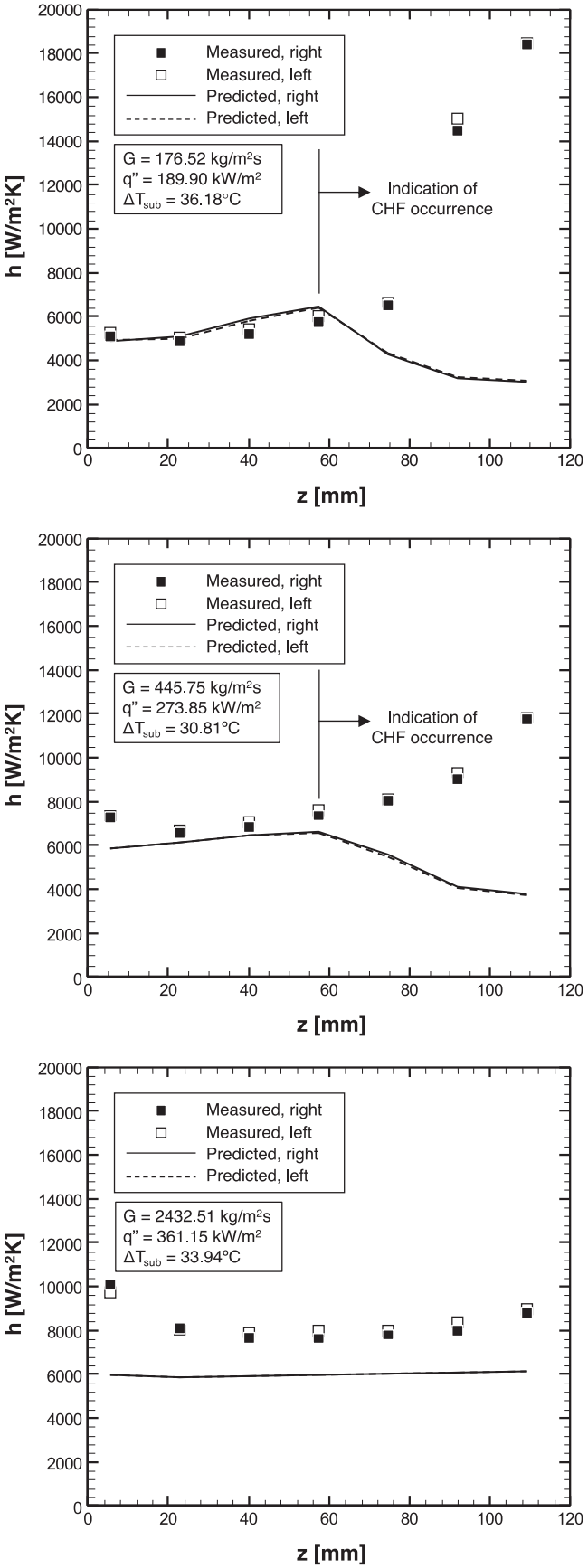

Fig. 12. Comparison of computationally predicted with experimentally measured heat transfer coefficient along the heated portion of the channel for different operating conditions.

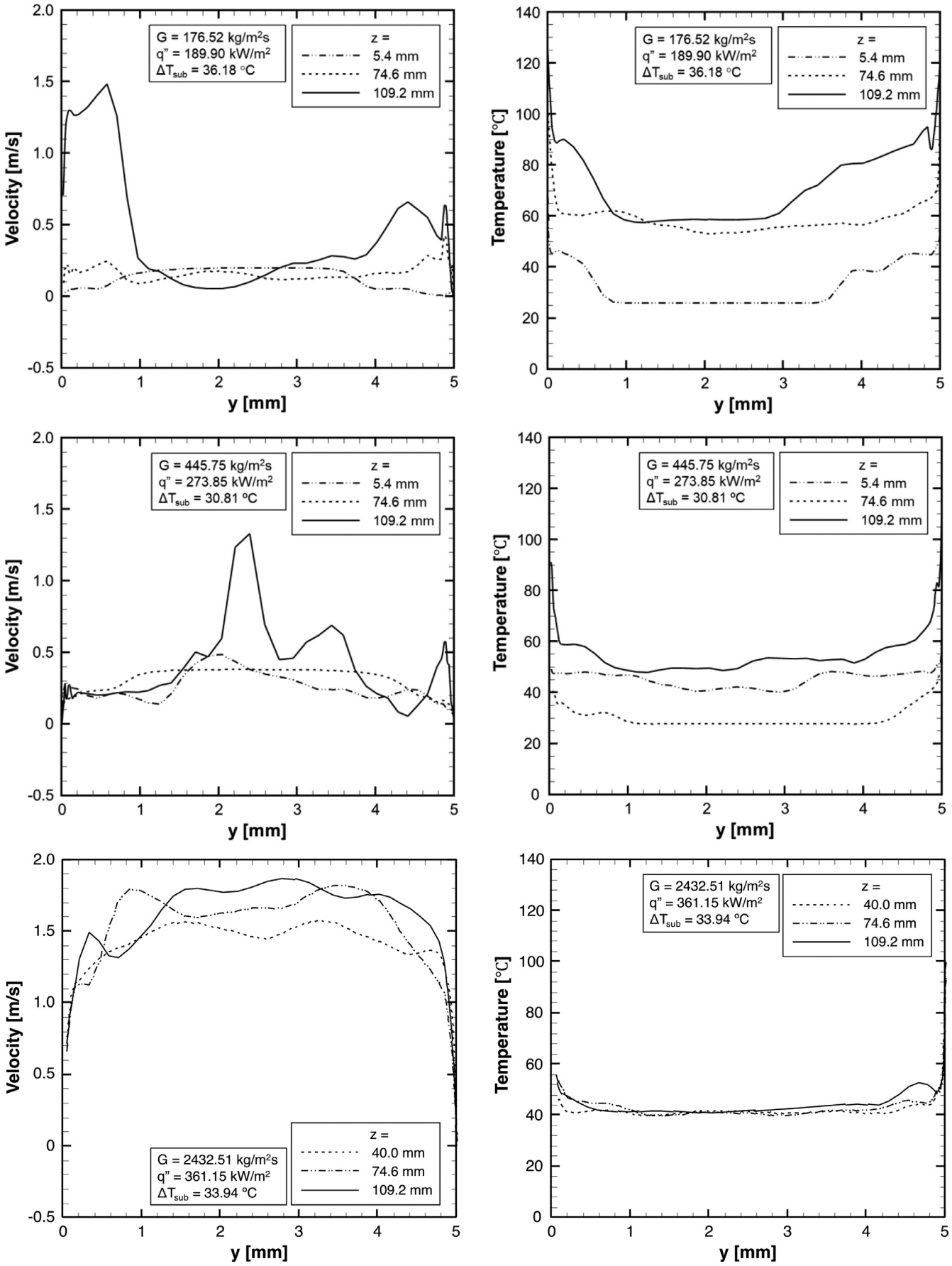

Fig. 13. Computationally predicted fluid velocity and fluid temperature profiles between heated walls at three axial measurement locations.

Fig. 11 shows local average fluid temperature along the heated length of the channel for each set of operating conditions tested, along with experimental results for measured inlet and exit fluid temperatures. Values taken from CFD simulations are instantaneous mass-weighted averages evaluated over the 2-D cross section at a given axial position.

In each case, it is clear fluid temperature increases near-linearly along the channel length, and the slope of this change increases after the new, higher heat flux is applied. The two lower mass velocity cases experience more temperature change and highest mass velocity case less due to larger differences in mass velocity than heat flux. Local temperature trends for the two lower mass velocity cases again show a strong change near the channel midpoint due to the large amount of vapor volume present downstream of that point.

Fig. 12 provides comparisons of computationally predicted and experimentally measured values of heat transfer coefficient for each case. Values are plotted for each of the seven axial measurement positions (thermocouple positions described in Fig. 1) to highlight local variations and the ability of the current computational approach to capture these. Reported values for the computational cases are calculated by dividing uniform heat flux by the difference between mean wall and fluid temperatures (averaged along the transverse direction). This is similar to the control-volume energy balance employed using experimental temperature measurements and makes for a valid comparison between the two.

Predictions for the highest mass velocity case of $G = 2432.51$ kg/m^{2}s show experimental results are underpredicted along the entire channel length. Experimentally, heat transfer coefficient is seen to initially decrease with axial position before once again increasing near the exit region, a trend which is not captured by computational simulations for these high mass velocity cases.

The two lower mass velocity cases of $G = 176.52$ kg/m^{2}s and $G = 445.75$ kg/m^{2}s, meanwhile, show good agreement between measured and predicted heat transfer coefficient in the upstream region. There is a sharp departure near the channel midsection, however, after which experimental values of heat transfer coefficient increase while predicted values decrease. Decreasing values of heat transfer coefficient are a result of vapor accumulation in the computational cases and are a key sign CHF is occurring in these cases.

Finally, Fig. 13 provides fluid velocity and fluid temperature profiles between the heated surfaces at three different axial positions for each set of operating conditions investigated. Each set of plots corresponds to conditions at the end of the current transient analysis, and are instantaneous.

For the two lower mass velocity cases, appreciable variations are seen in both velocity and temperature profiles, particularly in the downstream portion of the channel. These are due to the presence of significant vapor for these cases leading to strong local variations in both thermal and hydrodynamic behavior (as discussed in conjunction of many of the prior plots).

All but the highest mass velocity case show temperature peaks well above saturation (~62.19 °C) in the near wall region towards the channel exit, indicating vapor has blanketed the heated surfaces. Velocity peaks are also seen in these regions due to the presence of fast-moving vapor. This further reinforces the idea these computational cases are experiencing CHF.

The highest mass velocity case with $G = 2432.51$ kg/m^{2}s shows much smoother velocity and temperature profiles due to the significantly reduced void fraction values. Temperature profiles show saturation is only reached very close to the wall, and there is no appreciable vapor superheat. This is in stark contrast to lower velocity cases were significant vapor superheat is observed and superheated vapor layers extend 1-2 mm towards the channel centerline.

4.3. Premature prediction of CHF

Noticeable throughout the present work is some underprediction of CHF by computational methods compared to experimental results. Although heat flux levels investigated here are relatively close to experimental CHF values (within ~18%, on average), it is expected further refinement to mass transfer modeling will bring predicted results much closer to experimental observations.

Key targets for future investigation are 1) mass transfer intensity factor r_i used for boiling, and 2) r_i used for condensation. In an early 2-D computational study by the present authors [34], it was seen boiling r_i needed to be tuned for individual combinations of flowrate and heat flux to yield optimal predictive results. Further, while it is acceptable to employ low value for condensation r_i for low heat flux boiling cases, this may not be appropriate for heat fluxes nearing CHF. This indicates r_i for condensation must be increased in order to tackle pre-CHF cases. Further exploration of this is expected to be a key focus of future work by the current authors focused on accurate prediction of CHF using computational methods.

Furthermore, the multiphase model could be improved by mathematically considering a set of conservation, momentum, and energy equations for each phase for better prediction of local secondary flow surrounding vapor bubbles attached to or departed from the surface, along with reliable modeling of bubble nucleation and dynamics. Accurate prediction of local fluid field is also important, affecting the interfacial configuration, momentum transfer, and rate of phase change. In addition, the numerical scheme for the phase change and interface reconstruction could be improved upon. As phase change takes place, volume of fraction of the vapor phase in a cell increases from 0 to 1 with time (in the transient analysis), and this transition is numerically necessary to avoid trivial solution or divergence, and to differentiate variables (in the actual phenomena, only 0 and 1 exist). However, this manipulation causes inevitable deviation when computing properties, leading to less accurate prediction of momentum along the interface and heat transfer by sensible and latent heat. Such improvements will undoubtedly require considerable endeavor to mathematically and numerically develop the scheme used, let alone the need for abundant computer resources.

But despite these shortcomings, the present computational work does demonstrate the ability to effectively predict the degradation in heat transfer performance commonly encountered at heat fluxes nearing CHF.

5. Conclusions

The present study employed computational methods to explore local heat transfer and hydrodynamic behavior just prior to and during the CHF transient. Conditions correspond to experimental data collected for highly subcooled vertical upflow boiling of FC-72 in a 2.5 mm x 5 mm rectangular channel. Experimental flow visualization and temperature results for accompanying pre-CHF cases were provided for comparison with predicted results.

Key outcomes include the important influence of shear-lift force generated by velocity gradients towards sidewalls in driving vapor towards the channel centerline. Strong local variations in heat transfer from the heated surface were also observed for cases undergoing the CHF transient. Use of ANSYS-Fluent to elucidate critical local information not readily available using traditional experimental methods represents another step forward for two-phase computational methods. Specific findings from the study are:

1) The current computational scheme is successful in capturing key two-phase flow phenomena including nucleation, bubble sliding and departure, coalescence, and vapor breakup. Use of a

3-D domain and additional shear-lift force modeling are shown to provide key benefits for physical prediction of two-phase flow heat transfer and hydrodynamic behavior.

2) Shear-lift force acting from channel sidewalls is seen to drive vapor towards the channel centerline, leading to peak heat transfer rates near the channel corners (away from vapor accumulation). This outcome shows the potential of two-phase CFD to elucidate complex local behaviors present in flow boiling not easily determined using traditional experimental methods.
3) Lower mass velocity cases investigated here show clear signs of vapor blanketing heated walls and rapid temperature rise commonly associated with onset of CHF. The Highest mass velocity case indicates flow is still pre-CHF, and although signs of vapor accumulation are present, the CHF transient is not encountered.
4) Although predicting CHF somewhat earlier than encountered experimentally, the current computational approach is shown to be a powerful tool for identifying pre-CHF behavior and analyzing local behavior during the CHF transient. It is expected additional refinements to mass transfer modeling will lead to better agreement between computational and experimental CHF values.

Declaration of Competing Interest

The authors declare that they have no known competing financial interests or personal relationships that could have appeared to influence the work reported in this paper.

Acknowledgements

The authors are grateful for financial support provided by the National Aeronautics and Space Administration (NASA) under grant no. NNX17AK98G, and technical support of the NASA Glenn Research Center, Cleveland, Ohio.

References

[1] T.J. LaClair, I. Mudawar, Thermal transients in a capillary evaporator prior to the initiation of boiling, Int. J. Heat Mass Transfer 43 (2000) 3937–3952.
[2] I. Mudawar, T.M. Anderson, Parametric investigation into the effects of pressure, subcooling, surface augmentation and choice of coolant on pool boiling in the design of cooling system for high-power-density electronic chips, J. Electronic Packaging 112 (1990) 375–382.
[3] I. Mudawar, T.M. Anderson, Optimization of extended surfaces for high flux chip cooling by pool boiling, J. Electronic Packaging 115 (1993) 89–100.
[4] J.A. Shmerler, I. Mudawar, Local evaporative heat transfer coefficient in turbulent free-falling liquid films, Int. J. Heat Mass Transfer 31 (1988) 731–742.
[5] T.H. Lyu, I. Mudawar, Statistical investigation of the relationship between interfacial waviness and sensible heat transfer to a falling liquid film, Int. J. Heat Mass Transfer 34 (1991) 1451–1464.
[6] I. Mudawar, R.A. Houpt, Measurement of mass and momentum transport in wavy-laminar falling liquid films, Int. J. Heat Mass Transfer 36 (1993) 4151–4162.
[7] D. Maddox, I. Mudawar, Single- and two-phase convective heat transfer from smooth and enhanced microelectronic heat sources in a rectangular channel, J. Heat Transfer 111 (1989) 1045–1052.
[8] T.C. Willingham, I. Mudawar, Forced-convection boiling and critical heat flux from a linear array of discrete heat sources, Int. J. Heat Mass Transfer 35 (1992) 2879–2890.
[9] J.C. Sturgis, I. Mudawar, Critical heat flux in a long, rectangular channel subjected to one-sided heating - II. Analysis of CHF data, Int. J. Heat Mass Transfer 42 (1999) 1849–1862.
[10] C.O. Gersey, I. Mudawar, Effects of heater length and orientation on the trigger mechanism for near-saturated flow boiling CHF - I. Photographic and statistical characterization of the near-wall interfacial features, Int. J. Heat Mass Transfer 38 (1995) 629–642.
[11] W. Qu, I. Mudawar, S.Y. Lee, S.T. Wereley, Experimental and computational investigation of flow development and pressure drop in a rectangular micro-channel, J. Electronic Packaging 128 (2006) 1–9.
[12] S. Mukherjee, I. Mudawar, Smart, low-cost, pumpless loop for micro-channel electronic cooling using flat and enhanced surfaces, in: Proc. I-Therm 2002: Int. Conf. Thermal, Mechanics and Thermomechanical Phenomena in Electronic Systems, San Diego, California, 2002, pp. 360–370. May 29-June 1, 2002.
[13] S. Mukherjee, I. Mudawar, Pumpless loop for narrow channel and micro-channel boiling from vertical surfaces, J. Electronic Packaging 125 (2003) 431–441.
[14] D.C. Wadsworth, I. Mudawar, Enhancement of single-phase heat transfer and critical heat flux from an ultra-high-flux simulated microelectronic heat source to a rectangular impinging jet of dielectric liquid, J. Heat Transfer 114 (1992) 764–768.
[15] M.E. Johns, I. Mudawar, An ultra-high power two-phase jet-impingement avionic clamshell module, J. Electronic Packaging 118 (1996) 264–270.
[16] W.P. Klinzing, J. Rozzi, I. Mudawar, Film and transition boiling correlations for quenching of hot surfaces with water sprays, J. Heat Treating 9 (1992) 91–103 1992.
[17] M.K. Sung, I. Mudawar, Single-phase and two-phase heat transfer characteristics of low temperature hybrid micro-channel/micro-jet impingement cooling module, Int. J. Heat Mass Transfer 51 (2008) 3882–3895.
[18] J. Donea, S. Giuliani, J.P. Halleux, An arbitrary Lagrangian-Eulerian finite element method for transient dynamic fluid-structure interactions, Comput. Methods Appl. Mech. Eng. 33 (1982) 689–723.
[19] C.W. Hirt, A.A. Amsden, J.L. Cook, An arbitrary Lagrangian-Eulerian computing method for all flow speeds, J. Comput. Phys. 14 (1974) 27–253.
[20] T. Sun, W. Li, S. Yang, Numerical simulation of bubble growth and departure during flow boiling period by lattice Boltzmann method, Int. J. Heat Fluid Flow 44 (2013) 120–129.
[21] W.H. Lee, A pressure iteration scheme for two-phase flow modeling, multiphase transport: fundamentals, reactor safety, Applications 1 (1980) 407–431.
[22] R.W Schrage, A Theoretical study of interphase mass transfer, Columbia University Press, New York, 1953.
[23] H. Pothukuchi, S. Kelm, B.S.V. Patnaik, B.V.S.S.S. Prasad, H.J. Allelein, CFD modeling of critical heat flux in flow boiling: validation and assessment of closure models, Applied Thermal Eng 150 (2019) 651–665.
[24] Q. Li, M. Avramova, Y. Jiao, P. Chen, J. Yu, Z. Pu, J. Chen, CFD prediction of critical heat flux in vertical heated tubes with uniform and non-uniform heat flux, Nuclear Eng. Design 326 (2018) 403–412.
[25] D.L. Youchison, M.A. Ulrickson, J.H. Bullock, Prediction of critical heat flux in water-cooled plasma facing components using computational fluid dynamics, Fusion Sci. Tech 60 (2011) 177–184.
[26] S. Mimouni, C. Baudry, M. Guingo, J. Lavieville, N. Merigoux, N. Mechitoua, Computational multi-fluid dynamics predictions of critical heat flux in boiling flow, Nuclear Eng. Design 299 (2016) 28–36.
[27] L. Vyskocil, J. Macek, CFD simulation of critical heat flux in a tube, CFD for Nuclear Reactor Safety Applications OECD/NEA and IAEA (2010) 1–13.
[28] H. Li, S.A. Vasquez, H. Punekar, R. Muralikrishnan, Prediction of boiling and critical heat flux using an Eulerian multiphase boiling model, ASME Int. Mechanical Eng. Congress and Exposition (2012) 463–476.
[29] A. Sokolichin, G. Eigenberger, Dynamic numerical simulation of gas-liquid two-phase flows Euler/Euler versus Euler/Lagrange, Chem. Eng. Sci. 52 (1997) 611–626.
[30] D. Pfleger, S. Gomes, N. Gilbert, H.-G Wagner, Hydrodynamic simulations of laboratory scale bubble columns fundamental studies of the Eulerian-Eulerian modelling approach, Chem. Eng. Sci. 54 (1999) 5091–5099.
[31] L.E. O'Neill, I. Mudawar, M.M. Hasan, H.K. Nahra, R. Balasubramaniam, N.R. Hall, N.R. Hall, A. Lokey, J.R. Mackey, Experimental investigation into the impact of density wave oscillations on flow boiling system dynamic behavior and stability, Int. J. Heat Mass Transfer 120 (2018) 144–166.
[32] D.L. Youngs, Time-dependent multi-material flow with large fluid distortion, Numerical Methods for Fluid Dynamics, Academic Press, 1982.
[33] J.U. Brackbill, D.B. Kothe, C. Zemach, A continuum method for modeling surface tension, J. Comput. Phys. 100 (1992) 335–354.
[34] J. Lee, L.E. O'Neill, S. Lee, I. Mudawar, Experimental and computational investigation on two-phase flow and heat transfer of highly subcooled flow boiling in vertical upflow, Int. J. Heat Mass Transfer 136 (2019) 1199–1216.
[35] J. Lee, L.E. O'Neill, I. Mudawar, 3-D computational investigation and experimental validation of effect of shear-lift on two-phase flow and heat transfer characteristics of highly subcooled flow boiling in vertical upflow, Int. J. Heat Mass Transfer 150 (2020) 119291.
[36] J.F. Klausner, R. Mei, D.M. Bernhard, L.Z. Zeng, Vapor bubble departure in forced convection boiling, Int. J. Heat Mass Transfer 36 (1993) 651–662.
[37] I. Mudawar, C.H. Lee, A mechanistic critical heat flux model for subcooled flow boiling based on local bulk flow conditions, Int. J. Multiphase Flow 14 (1988) 711–728.
[38] J.E. Galloway, I. Mudawar, CHF mechanism in flow boiling from a short heated wall-I. examination of near-wall conditions with the aid of photomicrography and high-speed imaging, Int. J. Heat Mass Transfer 36 (1993) 2511–2526.
[39] C.R. Kharangate, L.E. O'Neill, I. Mudawar, Effects of two-phase inlet quality, mass velocity, flow orientation, and heating perimeter on flow boiling in a rectangular channel: Part 2 - CHF experimental results and model, Int. J. Heat Mass Transfer 103 (2016) 1280–1296.
[40] J. Lee, D. Jo, H. Chae, S.H. Chang, Y.H. Jeong, J.J. Jeong, The characteristics of premature and stable critical heat flux for downward flow boiling at low pressure in a narrow rectangular channel, Exp. Thermal Fluid Sci. 69 (2015) 86–98.
[41] I. Mudawar, J.E. Galloway, CHF mechanism in flow boiling from a short heated wall-II. theoretical CHF model, Int. J. Heat Mass Transfer 36 (1993) 2527–2540.